# Initial Oxygen Incorporation in the Prismatic Surfaces of Troilite FeS

Umberto Terranova,*[ORCID] Claire Mitchell, Meenakshisundaram Sankar, David Morgan,[ORCID] and Nora H. de Leeuw*[ORCID]

School of Chemistry, Cardiff University, Cardiff CF10 3AT, U.K.

ABSTRACT: We present a theoretical investigation of the prismatic $(01\bar{1}0)$ surface of troilite in an oxidizing environment, which aims to elucidate the presence of oxygen detected experimentally in the pyrrhotite $Fe_{1-x}S$ nanoparticles. We find that atomic oxygen adsorbs in Fe−O−Fe bridging motifs, which are thermodynamically stable under ambient conditions. During the first oxidation steps, the formation of the S−O bond is less favored than Fe−O, suggesting that the sulfur oxides detected experimentally form only subsequently. We predict, moreover, that substitution of sulfur for oxygen can occur. The appearance of Fe−O−Fe−O−Fe bridging motifs due to successive adsorptions points toward a clustering growth of the oxidic units. In agreement with the experimental observations, the oxidation of troilite is exothermic, where the equilibrium between adsorption and substitution is influenced by the presence of Fe vacancies.
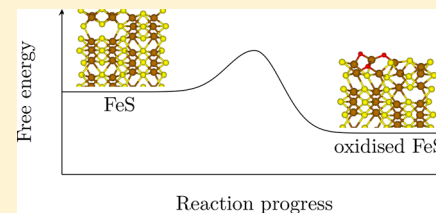
1. INTRODUCTION

Iron sulfide surfaces play a pivotal role in a number of significant environmental processes. Their exposure to air and water is responsible for the harmful formation of acid mine drainage.[1] In aqueous solution, they can adsorb heavy metals and radionuclides, thereby providing an effective solution to the remediation of polluted water.[2−7] Considerable interest has been devoted to the role of iron sulfides as possible catalysts in the formation of the first organic compounds at hydrothermal vents,[8−11] where the formation of mackinawite FeS has been revealed in experiments simulating chimney growth under early Earth conditions.[12] On the basis of this attractive hypothesis, the reduction of carbon dioxide to organic molecules has been demonstrated to occur under ambient conditions on greigite Fe_3S_4.[13]

Pyrrhotites $Fe_{1-x}S$ ($0 \leq x \leq 0.125$), the most common iron sulfides in nature after pyrite FeS_2, hold great potential as catalysts. In particular, both molecular hydrogen[14] and oxygen[15] evolution, as well as the hydrogenation of azobenzenes,[16] have recently been shown to occur on their surfaces.

Like pyrite, pyrrhotites are very reactive toward molecular oxygen, which is easily incorporated into their surfaces.[17−21] In order for the catalytic mechanisms to be understood properly, we need to achieve a detailed knowledge of the oxidized substrate available to the reactants after exposure to ambient air. However, contrary to pyrite,[22−29] theoretical investigations of pyrrhotite surfaces are scarce[30] and none exist to the authors' knowledge on their oxidation.

Here, after synthesizing pyrrotite nanoparticles and using X-ray photoelectron spectroscopy (XPS) to show that the catalytically relevant surfaces contain Fe−O and SO_x species, we use density functional theory (DFT) to study the early oxidation mechanism of the prismatic surfaces of troilite FeS (i.e., the stoichiometric end-member of the pyrrhotite group). In agreement with experiment, we find that the incorporation of oxygen is thermodynamically favored, with a tendency for

the oxidic units to grow in clusters. We also discuss how Fe vacancies affect the oxidation mechanism.

2. METHODS

2.1. Ab initio Thermodynamics. The free energy γ of a surface in equilibrium with particles acting as reservoirs can be expressed under given thermodynamic conditions of temperature T and pressure p as[31]

$$\gamma = \frac{1}{A}\left(G(T, p) - \sum_i N_i\mu_i(T, p)\right) \quad (1)$$

where G is the Gibbs free energy of the solid exposing the surface A, and N_i and μ_i are the number and chemical potentials of species i, respectively.

$$G(p, T) = F(V, T) + pV \quad (2)$$

Following eq 1, the free energy of a troilite surface interacting with molecular oxygen becomes

$$\gamma = \frac{1}{2A}(G_{slab} - N_{Fe}\mu_{Fe} - N_S\mu_S - N_O\mu_O) \quad (3)$$

where G_{slab} is the Gibbs free energy of the surface slab and the factor 2 takes into account its symmetric terminations. We note that μ_{Fe} and μ_S cannot be independent, as Fe and S particles are in equilibrium with bulk FeS, which acts as the thermodynamic reservoir:

$$\mu_{Fe} + \mu_S = g_{FeS} \quad (4)$$

where g_{FeS} is the Gibbs free energy per formula unit of troilite. We can use eq 4 to remove the dependence of γ on μ_{Fe} in eq 3:

$$\gamma = \frac{1}{2A}(G_{\text{slab}} - N_{\text{Fe}}g_{\text{FeS}} + (N_{\text{Fe}} - N_{\text{S}})\mu_{\text{S}} - N_{\text{O}}\mu_{\text{O}}) \quad (5)$$

The oxygen chemical potential, μ_{O}, can be expressed as[32]

$$\mu_{\text{O}}(T, p) = 1/2(E_{\text{O}_2} + \tilde{\mu}_{\text{O}_2}(T, p^0) + kT\ln(p/p^0)) \quad (6)$$

where E_{O_2} is the DFT energy of the oxygen molecule, which includes a +0.81 eV term correcting the overestimation of the O_2 binding energy by the PBE functional,[33] and p^0 is a reference pressure. All the temperature-dependent contributions are included in $\tilde{\mu}_{\text{O}_2}$, which can be derived by using the tabulated enthalpy and entropy values at $p^0 = 1$ atm.[34] Under conditions of room temperature and pressure ($T = 300$ K and $p = 1$ atm), μ_{O} corresponds to −4.80 eV.

The sulfur chemical potential cannot vary without bounds. At sufficiently high values of μ_{S}, orthorhombic S_8 will start to form, which sets the upper bound limit:

$$\mu_{\text{S}} \leq 1/8g_{S_8} \quad (7)$$

while eq 4 together with the condition that metallic Fe does not form imply that

$$\mu_{\text{S}} \geq g_{\text{FeS}} - g_{\text{Fe}} \quad (8)$$

where g_{S_8} and g_{Fe} are the Gibbs free energy per formula unit of orthorhombic S_8 and metallic Fe, respectively. Equations 7 and 8 determine the values of the S-rich and S-poor conditions, respectively.

The Gibbs free energy of the solid species can be decomposed as

$$G = E + F^{\text{vib}} + pV \quad (9)$$

where E is the electronic energy and F^{vib} the vibrational term. In this work, we have neglected the vibrational and the pV contributions. Equation 5 therefore becomes

$$\gamma = \frac{1}{2A}(E_{\text{slab}} - N_{\text{Fe}}E_{\text{bulk}} + (N_{\text{Fe}} - N_{\text{S}})\mu_{\text{S}} - N_{\text{O}}\mu_{\text{O}}) \quad (10)$$

where E_{slab} and E_{bulk} are the DFT energies of the slab and per formula unit of troilite, respectively.

2.2. Computational Details. All geometry optimizations were performed with VASP 5.3[35,36] using the PBE functional[37] and the same U parameter of 1 eV as in previous works on troilite.[38,39] We have employed the projector augmented wave method to model the core−electron interaction,[40] treating explicitly the 4s, 3d, and 3p electrons of Fe and the 3s and 3p of S. The spin configuration of troilite, antiferromagnetic along the c axis,[41] was used for all surfaces. The optimizations were performed with a plane wave cutoff of 400 eV, which guarantees that absolute energies of bulk troilite are converged within 1 meV per formula unit and stopped when the forces acting on the ions were less than 10^{-2} eV/Å. After finding that a 4 × 4 × 2 Monkhorst−Pack grid[42] ensures that absolute energies of bulk troilite are converged to better than 1 meV per formula unit, we scaled the grids of the surface calculations inversely with the dimension of the unit cells. Surface slabs were separated by a vacuum region of 16 Å along the normal direction. All structures were drawn with VESTA.[43]

2.3. Synthesis and Characterization of $Fe_{1−x}S$. $Fe_{1−x}S$ was synthesized by a method reported by Beal et al.,[44] using iron(II) acetylacetonate ($Fe(acac)_2$) (Molekula), sulfur (sublimed) (Alfa Aesar), and oleylamine (OAm) (70%) (Sigma).

Reactions were carried out in a three-necked flask equipped with a condenser, temperature probe, and magnetic stir bar. OAm was initially degassed by bubbling nitrogen rapidly through for 30 min, and the reaction was carried out under a nitrogen atmosphere. $Fe(acac)_2$ (0.77 g, 3 mmol) and sulfur (0.098 g, 3 mmol) were placed in a flask and flushed with nitrogen. The degassed OAm (60 cm³) was added and stirred to produce a dark red suspension. While constantly bubbling nitrogen through the reaction mixture, the suspension was rapidly heated to the reaction temperature and held for a certain amount of time before being cooled to room temperature. Experiments were performed at either 280 or 310 °C, and the heating period was between 4 and 12 hours. To remove the OAm, acetone was added (40 cm³), followed by centrifugation and removal of the organic brown supernatant layer. To wash the black iron sulfide nanocrystals, the solid was then resuspended in toluene, followed by centrifugation. This step was repeated until the supernatant was clear and colorless. The sample was then left in a vacuum oven at room temperature overnight and stored as a powder.

X-ray powder diffraction (XRD) was performed on a PANalytical X'pert Pro powder diffractometer with a Ni filtered Cu $K\alpha$ radiation source operating at 40 keV and 40 mA. Patterns were recorded over the angular range 10−80 degrees, using a step size of 0.016 degrees. The XRD showed a well-crystallized sample, with a diffraction pattern that confirms the iron sulfide phase as $Fe_{1−x}S$, monoclinic pyrrhotite, ICDD 01−078−4315. Following the method reported by Yund and Hall,[45] which uses the d_{102} spacing to determine the Fe/S atomic ratio according to the equation:

$$\%\text{Fe} = 45.212 + 72.86(d_{102} - 2.0400) + 311.5(d_{102} - 2.0400)^2 \quad (11)$$

we estimated our sample to be $Fe_{0.94}S$.

2.4. X-ray Photoelectron Spectroscopy. XPS was performed on a Thermo Fisher Scientific K-alpha+ spectrometer. Samples were analyzed using a microfocused monochromatic Al X-ray source (72 W) over an area of approximately 400 μm. Data were recorded at pass energies of 150 eV for survey scans and 40 eV for high-resolution scans with 1 and 0.1 eV step sizes, respectively. Charge neutralization of the sample was achieved using a combination of both low-energy electrons and argon ions. Data analysis was performed in CasaXPS using a Shirley type background and Scofield cross sections, with an energy dependence of −0.6. With the absence of mineral standards, the line shapes for Fe−S species were deduced from electronic spectra taken from the work by Shimada et al.[46] The S 2p spectrum was fitted with a doublet representing the characteristic spin−orbit splitting of S $2p_{3/2}$ and S $2p_{1/2}$ lines.

3. RESULTS AND DISCUSSION

3.1. Surfaces of Troilite. Troilite belongs to the hexagonal crystal system (space group $P\bar{6}2c$). Its crystal structure where Fe atoms are arranged in a distorted octahedral coordination is shown in Figure 1. The calculated lattice vectors a and c and the internal atomic positions of troilite which we have used to create all surface unit cells are in very good agreement with the experimental values (Table 1).

We can decompose the structure of troilite into four FeS layers (A, B, A′, and B′) along the [0001] direction or three FeS layers (C, D, and E) along the [01$\bar{1}$0] direction (Figure 2). Due to the existence of a glide plane α along the c axis, layers
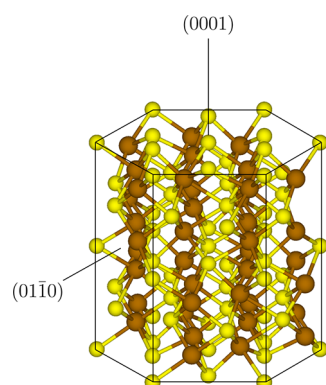
Figure 1. Crystal structure of troilite. The basal (0001) and the prismatic (01$\bar{1}$0) surfaces are shown. Color code: Fe, large brown spheres; S, small yellow spheres.

Table 1. Lattice Parameters and Internal Atomic Positions in Wyckoff Notation of Troilite

	this work	exp[47]
a (Å)	5.955	5.963
c (Å)	11.716	11.754
Fe(12i)	(0.3952, 0.0720, 0.1217)	(0.3787, 0.0553, 0.1230)
S(2a)	(0, 0, 0)	(0, 0, 0)
S(4f)	(1/3, 2/3, 0.0253)	(1/3, 2/3, 0.0208)
S(6h)	(0.6645, 0.0005, 1/4)	(0.6648, −0.0041, 1/4)

A′ and B′ are equivalent to A and B, respectively. Both Fe and S terminations of the (0001) surface can be obtained by expanding the slab symmetrically around the reflection plane β. Similarly, the terminations of the (01$\bar{1}$0) surface can be cut symmetrically around the glide plane α. The slabs of Figure 2 coincide with the A and C terminations of the (0001) and (01$\bar{1}$0) surfaces, respectively, employed in our calculations. It can easily be seen that terminations B, D, and E can be obtained by the symmetrical removal of one or more layers.

Contrary to the prismatic (01$\bar{1}$0), the basal (0001) surface of troilite is polar, which poses a significant challenge to the prediction of its termination. Polar surfaces exhibit a dipole moment which grows with the thickness of the slab and makes it unstable.[48] Unfortunately, no experimental data are available for the (0001) surface of troilite, which prompted us to introduce three nonpolar models following an approach based on the removal of surface atoms.[49−51] First, we constructed two 2 × 1 surface slabs (symmetric under reflection about the plane β) which terminated either with the S or the Fe atoms of layer A. Next, we removed symmetrically three of the six topmost atoms, thus attaining formal charge neutrality while eliminating the dipole from the slab.

The resulting S-terminated models are depicted in Figure 3. In A1, the removed S atoms belong to the same 1 × 1 unit cell, so that the two rows of S atoms running parallel to the [10$\bar{1}$0] direction are half occupied. In A2, every other row of S atoms which runs parallel to the [10$\bar{1}$0] direction is fully removed. In A3, only two of the three atoms of a row are removed, while the third is taken from the adjacent one. At this point, we should add that all the Fe-terminated slabs were unstable and relaxed into S-terminated ones.

Table 2 shows that all the (01$\bar{1}$0) terminations resulted in surface free energies which were between 25 and 30 meV/Å^2 lower than those of the (0001) surface models, although we cannot exclude the formation of other (0001) reconstructions
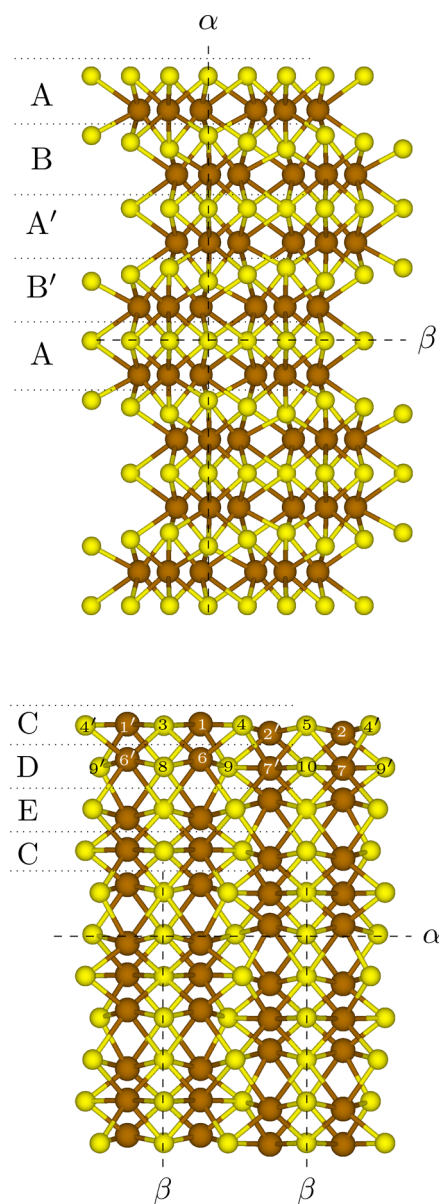

Figure 2. Structure of troilite decomposed into four FeS layers along the [0001] direction (top) and three FeS layers along the [01$\bar{1}$0] direction (bottom). The reflection planes β and the glide plane α are perpendicular to the plane of the screen with their normals perpendicular to the drawn lines. The glide direction is along the drawn line representing the plane α. The depicted slabs correspond to the terminations A and C employed in this work. In termination C, the symmetrically equivalent atoms are primed. Color code: Fe, large brown spheres; S, small yellow spheres.

with lower energies (Fe vacancies could for example contribute to their stabilization as in the Fe$_7$S$_8$ opposite end-member of pyrrhotites[30]). Termination C, in particular, has the lowest surface free energy.

Figure 4 shows the optimized structure of termination C. The relaxation from its bulk truncated structure depicted in Figure 2 is significant. Interestingly, the Fe6 atom of the subsurface layer presents the largest displacements. It moves upward by +0.97 Å, breaking the bonds with the sulfur atoms in the layer underneath and changing its geometry from octahedral to tetrahedral. While the relaxation of surface atoms along z is minor, it is not along the other two orthogonal
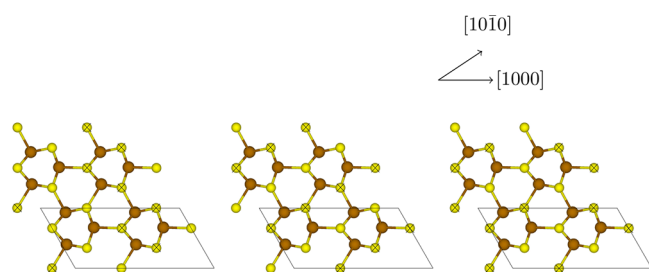
[10$\bar{1}$0]

[1000]

Figure 3. Models A1 (left panel), A2 (middle panel), and A3 (right panel) of the (0001) surface of troilite viewed along the c axis. The missing atoms and the surface unit cells are indicated. Only the topmost A layer is shown. Color code: Fe, large brown spheres; S, small yellow spheres.

Table 2. Free Energies γ (meV/Å^2) of the Different Terminations of the (0001) and (01$\bar{1}$0) Surfaces of Troilite

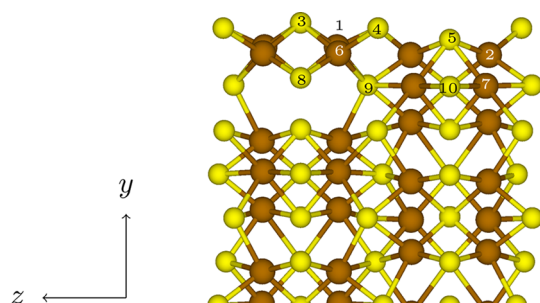| surface	termination	γ
(0001)	A1	49.7
	A2	47.6
	A3	49.1
(01$\bar{1}$0)	C	24.7
	D	27.2
	E	26.0

Figure 4. Relaxed structure of the (01$\bar{1}$0) termination C. Color code: Fe, large brown spheres; S, small yellow spheres.

directions. Finally, we mention that all the displacements vanish in the fourth layer, which confirms that our slab is thick enough to mimic bulk behavior. The atomic relaxations of termination C, hereafter employed to model the (01$\bar{1}$0) surface, are summarized in Table 3.

Table 3. Atomic Displacements (Å) of the C Termination of the (01$\bar{1}$0) Troilite Surface^a

layer	atom	dx	dy	dz
surface	Fe1	+0.20	−0.24	+0.08
	Fe2	−0.23	−0.17	−0.04
	S3	−0.55	+0.78	+0.00
	S4	+0.34	+0.56	+0.19
	S5	−0.32	+0.12	+0.00
subsurface	Fe6	−0.35	+0.97	+0.02
	Fe7	−0.07	+0.07	+0.09
	S8	−0.54	+0.32	+0.00
	S9	+0.07	+0.05	+0.00
	S10	−0.21	−0.02	+0.00

^{a}Labels refer to Figure 4.

3.2. Oxidised Surfaces. Figure 5 shows the Fe 2$p_{3/2}$ and S 2p XPS spectra of the Fe$_{1−x}$S nanoparticles, exposed to air for 3
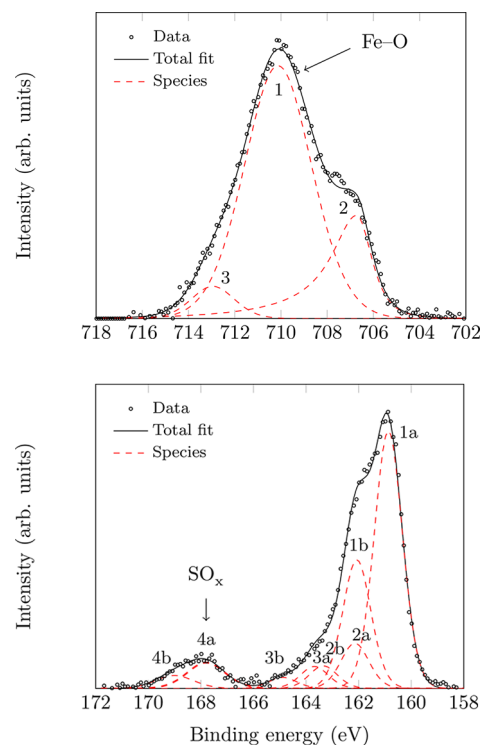

Figure 5. Fe 2$p_{3/2}$ (top) and S 2p (bottom) XPS spectra of the pyrrhotite nanoparticles. The peaks of the oxidic species are indicated by arrows.

Table 4. Interpretation of the XPS Spectra

XPS	peak	binding energy (eV)	area (%)	species
Fe 2$p_{3/2}$	1	710.1	10.71	Fe−O
	2	706.7	3.46	Fe−S
	3	713.0	0.58	satellite
S 2p	1a	160.9	14.19	$S^{2−}$
	1b	162.0	7.10	$S^{2−}$
	2a	162.1	2.49	$S_n^{2−}$
	2b	163.3	1.25	$S_n^{2−}$
	3a	163.7	1.22	$S_2^{2−}$
	3b	164.5	0.61	$S_2^{2−}$
	4a	167.8	1.94	SO_x
	4b	169.0	0.97	SO_x

days after their synthesis.[44] Table 4 reports the corresponding peak assignments. The Fe 2$p_{3/2}$ spectrum exhibits both Fe−S and Fe−O species, with the Fe−S component present at 706.7 eV, about 1 eV lower than that reported for Fe(II)−S bonds by Pratt et al.,[18] despite the S 2p peaks within experimental error. In the S 2p spectrum, we observe a dominance of monosulfides, followed by polysulfides and disulfides. Importantly, we detect the presence of SO_x species.

To shed light on the formation of the oxidic species, we have investigated the thermodynamics of the early oxidation of the (01$\bar{1}$0) troilite surface under ambient conditions. In doing so, besides the standard adsorption of oxygen atoms, we have also taken into account their incorporation by replacing sulfur

(which we have assumed to be released in its elemental form), as in a previous study explaining acid mine drainage caused by greigite.[52] Similarly, the substitution of sulfur for oxygen contributes to the oxidation of molybdenum disulfide.[53,54]

3.2.1. One Oxygen atom. First, we have adsorbed a single oxygen atom in two different Fe–O–Fe bridging geometries (*a* and *b*, Table 5). Despite the similar arrangement, their surface

Table 5. Geometries and Surface Free Energies γ (meV/Å^2) of Troilite Structures Incorporating One Oxygen atom[a]

label	bonding or substitution		γ(S-poor)	γ(S-rich)
a	Fe1′–O1–Fe1		−5.0	−5.0
b	Fe1–O1–Fe2′		+2.2	+2.2
c	Fe1–O1–Fe2′	S4–O1	+5.6	+5.6
d	S3–O1		+20.2	+20.2
e	S5–O1		+20.3	+20.3
f	S3→O1		+11.4	+23.5
g	S4→O1		−1.6	+10.5
h	S5→O1		+3.5	+15.6

[a]Fe and S labels refer to the bottom panel of Figure 2.

free energies differ by about 7 meV/Å^2 in favor of *a*. Next, we have relaxed three other geometries involving a S–O bond. In structure *c*, the oxygen atom bonds in a triple bridging mode by adding to the Fe–O–Fe coordination a third S–O bond, while in *d* and *e*, we have tested the adsorption on top of a sulfur atom. We note that compared to the bridging adsorptions, all those with the S–O bond are less favored. While our XPS measurements have detected both Fe–O and SO$_x$ species, the clear preference for the Fe–O–Fe coordination suggests that Fe–O species are the first to form on the $(01\bar{1}0)$ surface of troilite. The late formation of the S–O bond marks a significant difference between the $(01\bar{1}0)$ surface of troilite and the major (100) surface of pyrite.[27,29]

Next, we have studied all the possible replacements of a surface sulfur with an oxygen (*f*–*h*, Table 5). In the most stable structure, *g*, the oxygen occupies the S4 site in the bottom panel of Figure 2. However, the top panel of Figure 6 shows that, in the entire range of the allowed sulfur chemical potential, configuration *g* is less favored than the Fe–O–Fe bridging structure *a*, which we illustrate in the top panel of Figure 7. In summary, we suggest that the oxidation of the $(01\bar{1}0)$ surface of troilite starts with the formation of Fe–O–Fe bridging structures.

3.2.2. Two Oxygen Atoms. Starting from the most stable structure *a*, we have proceeded with the incorporation of a second oxygen atom. As listed in Table 6, we have relaxed a structure with a Fe–O–Fe–O–Fe bridging configuration (*a*) and a second with two separate Fe–O–Fe geometries (*b*). In addition, we have considered two further structures with a molecular oxygen between two adjacent Fe, either in a Fe–O–O–Fe bridging (*c*) or in a vertical configuration (*d*). An additional structure *e* differs from *a* as the second oxygen atom is also bonded to a sulfur atom (i.e., it is in a triple bridging configuration). Structure *a* is the most stable among the five investigated, with a difference of around 8 meV/Å^2 from *b*, which points toward a tendency of the bridging oxidic units to share the Fe atoms. In line with the results from the single atom incorporation, we find that the S–O bond, which we tested in structure *e*, does not form during the early oxidation. We note that both *c* and *d* are much higher in surface free energy than *a*
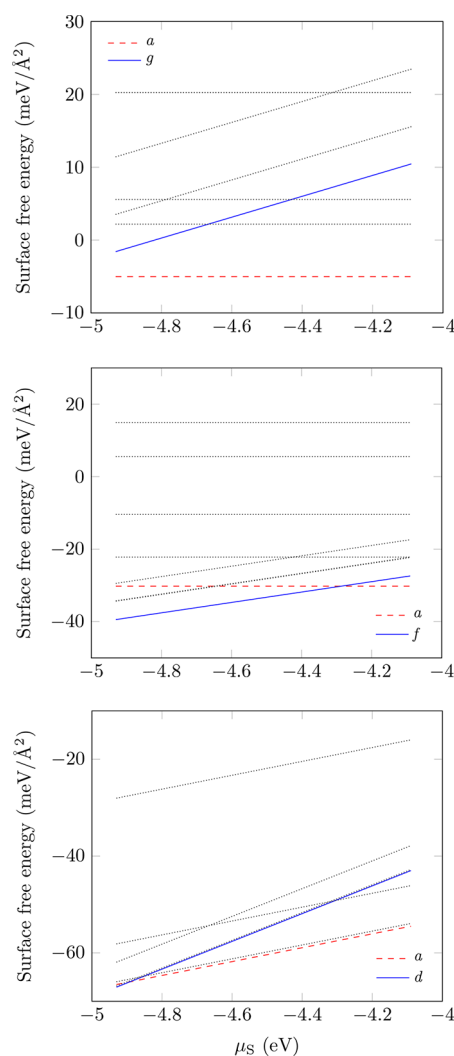

Figure 6. Surface free energies of the $(01\bar{1}0)$ termination of troilite with one (top), two (middle), and three (bottom) oxygen atoms incorporated either by adsorption or substitution. Only the values in the region of the allowed sulfur chemical potential are plotted. Dotted lines belong to the unfavorable adsorptions or substitutions.

and *b*, which suggests that the dissociation of any adsorbed molecular oxygen is a thermodynamically favored process.

Among all the possible substitution structures (*f*–*i*, Table 6), we find *f*, where the sulfur closest to the previously adsorbed oxygen is replaced, to be the most stable. Interestingly, the surface free energy curves in the middle panel of Figure 6 show that, with the exception of the most extreme region of the sulfur chemical potential, structure *f* is more favored than any adsorption, which confirms the significance of the oxidative substitution mechanism in iron sulfides.[52] We depict structure *f* in the middle panel of Figure 7.

3.2.3. Three Oxygen Atoms. In a similar fashion to the previous two oxidation steps, we have added a third oxygen atom to the most stable structure *f* discussed above. We have considered two different configurations obtainable by the addition of a second Fe–O–Fe bridging bond (Table 7). While configuration *a* contains a Fe–O–Fe–O–Fe bridge, in structure *b*, the two Fe–O–Fe units do not share a central Fe atom. Structure *a* has a lower surface free energy than *b*, which confirms the preference for the Fe–O–Fe–O–Fe motif found in the previous oxidation step. A third configuration *c*,
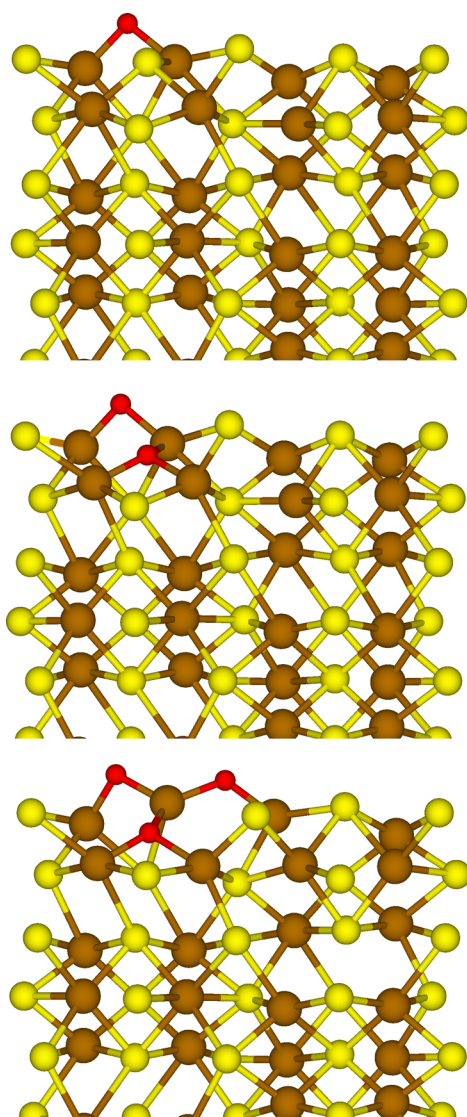
Figure 7. Most stable oxidized structures incorporating one (top), two (middle) and three (bottom) oxygen atoms. Color code: Fe, large brown spheres; S, small yellow spheres; and O, tiny red spheres.

where molecular oxygen is adsorbed in a Fe−O−O−Fe bridge on a structure containing a substituted sulfur, confirms the high penalty in surface free energy (38 meV/Å^2) for a structure with an undissociated O_2 molecule.

All possible configurations incorporating oxygen by a second sulfur substitution fall within a range of 5 meV/Å^2 (d−f, Table

7). As shown in the bottom panel of Figure 6, apart from the very small region below −4.9 eV, their surface free energy curves are always above that of structure a. The geometry of structure a, which we illustrate in the bottom panel of Figure 7, suggests that the clustering of the oxidic structures over the appearance of isolated Fe−O bonds is preferred from the very early stages of oxidation of troilite, a behavior similar to that observed during the oxidation of metals.[55]

The consistent decrease in the surface free energies with the addition of oxygen atoms, which can be appreciated by comparing the three plots of Figure 6, clearly indicates that these sulfide surfaces are only metastable in air, as they are increasingly stabilized by each oxidation step. In line with the XPS results, the initial oxidation of troilite is expected to be an exothermic process.

3.3. Role of Fe Vacancies. Fe vacancies are by far the most common defects in troilite. As such, we have investigated their stability on the (01$\bar{1}$0) surface and their effect on the incorporation of oxygen, limiting our analysis to the single atom adsorption.

Figure 8 illustrates the free energies of the clean and defective (01$\bar{1}$0) surfaces in the presence of Fe vacancies located in all possible sites of the surface and the subsurface layers (bottom panel of Figure 2). All the defective terminations present a stability window, which covers the entire range of the sulfur chemical potential in the case of Fe6 and Fe7 vacancies. This is a clear indication that troilite surfaces, regardless of the synthesis conditions, almost certainly will contain some Fe vacancies, in close agreement with experimental findings.[56]

At this point, we would like to discuss the effect of the vibrational contributions of the solid species, $\Delta F^{vib} = F^{vib}_{slab} - N_{Fe}F^{vib}_{bulk}$ to the energetics of the defects. We have used the harmonic approximation [i.e., $F^{vib} = \sum_i \log(2 \sinh(\hbar\omega_i/2k_BT))$] to estimate the vibrational terms of bulk troilite, and of the clean and Fe-defective (01$\bar{1}$0) surface, where ω_i are the phonon frequencies at the Γ-point. When simulating slabs, we have included in the Hessian matrix only the atoms of the three topmost FeS layers, which is consistent with our previous finding that all atomic displacements vanish in the fourth layer. We have found that the magnitude of ΔF^{vib} is less than 4 meV/Å^2 at room temperature, in line with the previous literature.[57,58] As a consequence, the conclusions drawn above on the stability of the defective terminations are not affected (inset of Figure 8), thus justifying the decision to neglect the vibrational terms throughout this work.

We have employed the most stable Fe6-deficient surface to study a number of oxygen incorporations in the proximity of the vacancy. In particular, we have relaxed the structures labeled

Table 6. Geometries and Surface Free Energies γ (meV/Å^2) of Troilite Structures Incorporating Two Oxygen atoms^a

label	bonding or substitution		γ(S-poor)	γ(S-rich)
a	Fe2−O1−Fe1′−O2−Fe1		−30.2	−30.2
b	Fe1′−O1−Fe1	Fe2′−O2−Fe2	−22.2	−22.2
c	Fe1′−O1−O2−Fe1		+5.6	+5.6
d	Fe1′−O1−Fe1	O1−O2	+15.0	+15.0
e	Fe1′−O1−Fe1−O2−Fe2′	S4−O2	−10.4	−10.4
f	Fe1′−O1−Fe1	S3→O2	−39.4	−27.4
g	Fe1′−O1−Fe1	S4′→O2	−34.4	−22.3
h	Fe1′−O1−Fe1	S4→O2	−34.2	−22.2
i	Fe1′−O1−Fe1	S5→O2	−29.4	−17.4

^{a}Fe and S labels refer to the bottom panel of Figure 2.

Table 7. Geometries and Surface Free Energies γ (meV/Å²) of Troilite Structures Incorporating Three Oxygen atoms[a]

label	bonding or substitution			γ(S-poor)	γ(S-rich)
a	Fe2−O1−Fe1′−O2−Fe1	S3→O3		−66.5	−54.5
b	Fe1′−O1−Fe1	Fe2′−O2−Fe2	S3→O3	−58.1	−46.1
c	Fe1′−O1−O2−Fe	S3→O3		−28.0	−16.0
d	Fe1′−O1−Fe1	S4′→O2	S3→O3	−67.1	−43.0
e	Fe1′−O1−Fe1	S4→O2	S3→O3	−66.9	−42.8
f	Fe1′−O1−Fe1	S5→O2	S3→O3	−61.9	−37.8

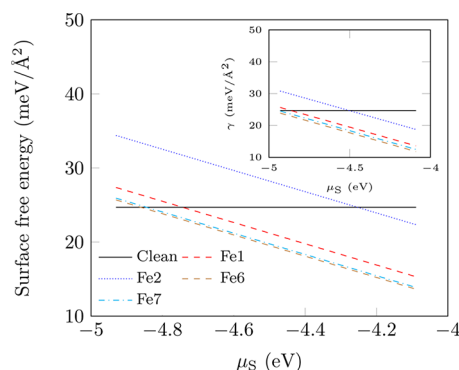[a]Fe and S labels refer to the bottom panel of Figure 2.

Figure 8. Free energies of the $(01\bar{1}0)$ surface of troilite with and without the presence of a Fe vacancy in the surface and the subsurface layers. Only the values in the region of the allowed sulfur chemical potential are plotted. Fe labels refer to the bottom panel of Figure 2. The inset shows the same curves after inclusion of the vibrational free energy terms.

in subsection 3.2.1 as *a* and *b* (Fe−O−Fe bonding), *d* (S−O bonding), *f* and *g* (sulfur substitutions), but with a vacancy in Fe6, and compared their surface free energies with those of the corresponding clean substrates. As illustrated in Figure 9,
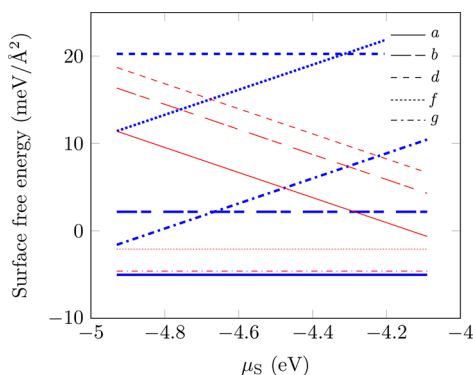

Figure 9. Free energies of the stoichiometric (thick blue lines) and defective (thin red lines) structures of the $(01\bar{1}0)$ troilite surface incorporating one oxygen atom. Only the values in the region of the allowed sulfur chemical potential are plotted. The structures are described in Table 5.

although still unfavorable compared to the Fe−O−Fe motifs, the formation of S−O bonds is significantly stabilized by the vacancy in the entire range of the allowed chemical potential. Interestingly, Fe vacancies penalize the adsorption of atomic oxygen in the bridging units while favoring the mechanism of sulfur substitution. As a result, in the Fe6-deficient surface slab, the free energy curves of configurations *f* and *g* lie below those of *a* and *b*, at odds with the stoichiometric case. Thus, a clear

effect emerges of Fe vacancies shifting the mechanism of oxygen incorporation toward the sulfur substitution.

4. CONCLUSIONS

The presence of Fe−O and SO_x species on the surface of $Fe_{1-x}S$ nanoparticles under oxidizing conditions, evidenced by XPS data, prompted us to undertake a theoretical investigation of the initial mechanisms of oxygen incorporation, which clarifies some fundamental processes occurring in the $(01\bar{1}0)$ surface of troilite FeS. We find that the oxidation is extremely exothermic and starts with the appearance of Fe−O−Fe motifs which tend to agglomerate even before the formation of the sulfur oxides observed by XPS.

Besides adsorption, our calculations suggest that oxygen atoms can be the result of sulfur replacement. In agreement with the experimental literature, we predict Fe vacancies to be stable, with a tendency to form in the subsurface layer. Fe vacancies contribute toward the stabilization of the S−O bond and, moreover, shift the mechanism of oxygen incorporation in favor of substitution, thus playing a key role during the early oxidation of troilite.

■ AUTHOR INFORMATION

Corresponding Authors
*E-mail: TerranovaU@cardiff.ac.uk.
*E-mail: deLeeuwN@cardiff.ac.uk.

ORCID
Umberto Terranova: 0000-0001-7380-4737
David Morgan: 0000-0002-6571-5731
Nora H. de Leeuw: 0000-0002-8271-0545

Notes
The authors declare no competing financial interest.

■ REFERENCES

(1) Singer, P. C.; Stumm, W. Acidic mine drainage: the rate-determining step. *Science* **1970**, *167*, 1121−1123.
(2) Moyes, L. N.; Parkman, R. H.; Charnock, J. M.; Vaughan, D. J.; Livens, F. R.; Hughes, C. R.; Braithwaite, A. Uranium uptake from aqueous solution by interaction with goethite, lepidocrocite, muscovite, and mackinawite: An X-ray absorption spectroscopy study. *Environ. Sci. Technol.* **2000**, *34*, 1062−1068.

(3) Bostick, B. C.; Fendorf, S. Arsenite sorption on troilite (FeS) and pyrite (FeS2). *Geochim. Cosmochim. Acta* **2003**, *67*, 909−921.

(4) Jeong, H. Y.; Klaue, B.; Blum, J. D.; Hayes, K. F. Sorption of mercuric ion by synthetic nanocrystalline mackinawite (FeS). *Environ. Sci. Technol.* **2007**, *41*, 7699−7705.

(5) Hyun, S. P.; Davis, J. A.; Sun, K.; Hayes, K. F. Uranium (VI) reduction by iron (II) monosulfide mackinawite. *Environ. Sci. Technol.* **2012**, *46*, 3369−3376.

(6) Lee, S. Y.; Baik, M. H.; Cho, H.-R.; Jung, E. C.; Jeong, J. T.; Choi, J. W.; Lee, Y. B.; Lee, Y. J. Abiotic reduction of uranium by mackinawite (FeS) biogenerated under sulfate-reducing condition. *J. Radioanal. Nucl. Chem.* **2013**, *296*, 1311−1319.

(7) Bone, S. E.; Bargar, J. R.; Sposito, G. Mackinawite (FeS) reduces mercury (II) under sulfidic conditions. *Environ. Sci. Technol.* **2014**, *48*, 10681−10689.

(8) Martin, W.; Russell, M. J. On the origins of cells: a hypothesis for the evolutionary transitions from abiotic geochemistry to chemo-autotrophic prokaryotes, and from prokaryotes to nucleated cells. *Philos. Trans. R. Soc., B* **2003**, *358*, 59−85.

(9) Mielke, R. E.; Robinson, K. J.; White, L. M.; McGlynn, S. E.; McEachern, K.; Bhartia, R.; Kanik, I.; Russell, M. J. Iron-sulfide-bearing chimneys as potential catalytic energy traps at life's emergence. *Astrobiology* **2011**, *11*, 933−950.

(10) Terranova, U.; de Leeuw, N. H. Structure and dynamics of water at the mackinawite (001) surface. *J. Chem. Phys.* **2016**, *144*, 094706.

(11) West, T.; Sojo, V.; Pomiankowski, A.; Lane, N. The origin of heredity in protocells. *Philos. Trans. R. Soc., B* **2017**, *372*, 20160419.

(12) White, L. M.; Bhartia, R.; Stucky, G. D.; Kanik, I.; Russell, M. J. Mackinawite and greigite in ancient alkaline hydrothermal chimneys: Identifying potential key catalysts for emergent life. *Earth Planet. Sci. Lett.* **2015**, *430*, 105−114.

(13) Roldan, A.; Hollingsworth, N.; Roffey, A.; Islam, H.-U.; Goodall, J. B. M.; Catlow, C. R. A.; Darr, J. A.; Bras, W.; Sankar, G.; Holt, K. B.; et al. Bio-inspired CO2 conversion by iron sulfide catalysts under sustainable conditions. *Chem. Commun.* **2015**, *51*, 7501−7504.

(14) Di Giovanni, C.; Wang, W.-A.; Nowak, S.; Greneche, J.-M.; Lecoq, H.; Mouton, L.; Giraud, M.; Tard, C. Bioinspired iron sulfide nanoparticles for cheap and long-lived electrocatalytic molecular hydrogen evolution in neutral water. *ACS Catal.* **2014**, *4*, 681−687.

(15) Chen, S.; Kang, Z.; Zhang, X.; Xie, J.; Wang, H.; Shao, W.; Zheng, X.; Yan, W.; Pan, B.; Xie, Y. Highly active Fe sites in ultrathin pyrrhotite Fe7S8 nanosheets realizing efficient electrocatalytic oxygen evolution. *ACS Cent. Sci.* **2017**, *3*, 1221−1227.

(16) Shao, Y.; Guo, Z.; Li, H.; Su, Y.; Wang, X. Atomic layer deposition of iron sulfide and its application as a catalyst in the hydrogenation of azobenzenes. *Angew. Chem.* **2017**, *129*, 3274−3279.

(17) Buckley, A.; Woods, R. X-ray photoelectron spectroscopy of oxidized pyrrhotite surfaces: I. Exposure to aire. *Appl. Surf. Sci.* **1985**, *22−23*, 280−287.

(18) Pratt, A.; Muir, I.; Nesbitt, H. X-ray photoelectron and Auger electron spectroscopic studies of pyrrhotite and mechanism of air oxidation. *Geochim. Cosmochim. Acta* **1994**, *58*, 827−841.

(19) Mikhlin, Y.; Varnek, V.; Asanov, I.; Tomashevich, Y.; Okotrub, A.; Livshits, A.; Selyutin, G.; Pashkov, G. Reactivity of pyrrhotite (Fe9S10) surfaces: spectroscopic studies. *Phys. Chem. Chem. Phys.* **2000**, *2*, 4393−4398.

(20) Janzen, M. P.; Nicholson, R. V.; Scharer, J. M. Pyrrhotite reaction kinetics: reaction rates for oxidation by oxygen, ferric iron, and for nonoxidative dissolution. *Geochim. Cosmochim. Acta* **2000**, *64*, 1511−1522.

(21) Belzile, N.; Chen, Y.-W.; Cai, M.-F.; Li, Y. A review on pyrrhotite oxidation. *J. Geochem. Explor.* **2004**, *84*, 65−76.

(22) Hung, A.; Muscat, J.; Yarovsky, I.; Russo, S. P. Density-functional theory studies of pyrite FeS2 (100) and (110) surfaces. *Surf. Sci.* **2002**, *513*, 511−524.

(23) Philpott, M. R.; Goliney, I. Y.; Lin, T. T. Molecular dynamics simulation of water in a contact with an iron pyrite FeS2 surface. *J. Chem. Phys.* **2004**, *120*, 1943−1950.

(24) von Oertzen, G. U.; Skinner, W. M.; Nesbitt, H. Ab initio and x-ray photoemission spectroscopy study of the bulk and surface electronic structure of pyrite (100) with implications for reactivity. *Phys. Rev. B: Condens. Matter Mater. Phys.* **2005**, *72*, 235427.

(25) Sit, P. H.-L.; Cohen, M. H.; Selloni, A. Interaction of oxygen and water with the (100) surface of pyrite: mechanism of sulfur oxidation. *J. Phys. Chem. Lett.* **2012**, *3*, 2409−2414.

(26) Zhang, G.; Al-Saidi, W.; Myshakin, E. M.; Jordan, K. D. Dispersioncorrected density functional theory and classical force field calculations of water loading on a pyrophyllite (001) surface. *J. Phys. Chem. C* **2012**, *116*, 17134−17141.

(27) Rozgonyi, T.; Stirling, A. DFT study of oxidation states on pyrite surface sites. *J. Phys. Chem. C* **2015**, *119*, 7704−7710.

(28) Stirling, A.; Rozgonyi, T.; Krack, M.; Bernasconi, M. Pyrite in contact with supercritical water: the desolation of steam. *Phys. Chem. Chem. Phys.* **2015**, *17*, 17375−17379.

(29) Dos Santos, E. C.; de Mendonca Silva, J. C.; Duarte, H. A. Pyrite oxidation mechanism by oxygen in aqueous medium. *J. Phys. Chem. C* **2016**, *120*, 2760−2768.

(30) Becker, U.; Munz, A. W.; Lennie, A. R.; Thornton, G.; Vaughan, D. J. The atomic and electronic structure of the (001) surface of monoclinic pyrrhotite (Fe7S8) as studied using STM, LEED and quantum mechanical calculations. *Surf. Sci.* **1997**, *389*, 66−87.

(31) Meyer, B. First-principles study of the polar O-terminated ZnO surface in thermodynamic equilibrium with oxygen and hydrogen. *Phys. Rev. B: Condens. Matter Mater. Phys.* **2004**, *69*, 045416.

(32) Reuter, K.; Scheffler, M. Composition, structure, and stability of RuO2 (110) as a function of oxygen pressure. *Phys. Rev. B: Condens. Matter Mater. Phys.* **2001**, *65*, 35406.

(33) Lee, Y.-L.; Kleis, J.; Rossmeisl, J.; Morgan, D. Ab initio energetics of LaBO3 (001) (B= Mn, Fe, Co, and Ni) for solid oxide fuel cell cathodes. *Phys. Rev. B: Condens. Matter Mater. Phys.* **2009**, *80*, 224101.

(34) Stull, D. R.; Prophet, H. *JANAF Thermochemical Tables*, 2nd ed.; National Standard Reference Data System; NSRDS-NBS 37; National Bureau of Standards, 1971.

(35) Kresse, G.; Hafner, J. Ab initio molecular dynamics for liquid metals. *Phys. Rev. B: Condens. Matter Mater. Phys.* **1993**, *47*, 558−561.

(36) Kresse, G.; Furthmuller, J. Efficiency of ab-initio total energy calculations for metals and semiconductors using a plane-wave basis set. *Comput. Mater. Sci.* **1996**, *6*, 15−50.

(37) Perdew, J. P.; Burke, K.; Ernzerhof, M. Generalized gradient approximation made simple. *Phys. Rev. Lett.* **1996**, *77*, 3865.

(38) Ricci, F.; Bousquet, E. Unveiling the room-temperature magnetoelectricity of troilite FeS. *Phys. Rev. Lett.* **2016**, *116*, 227601.

(39) Terranova, U.; de Leeuw, N. H. Phase stability and thermodynamic properties of FeS polymorphs. *J. Phys. Chem. Solids* **2017**, *111*, 317−323.

(40) Blöchl, P. E. Projector augmented-wave method. *Phys. Rev. B: Condens. Matter Mater. Phys.* **1994**, *50*, 17953.

(41) Martin, P.; Price, G.; Vočadlo, L. An ab initio study of the relative stabilities and equations of state of FeS polymorphs. *Mineral. Mag.* **2001**, *65*, 181−191.

(42) Monkhorst, H. J.; Pack, J. D. Special points for Brillouin-zone integrations. *Phys. Rev. B* **1976**, *13*, 5188.

(43) Momma, K.; Izumi, F. *VESTA3* for three-dimensional visualization of crystal, volumetric and morphology data. *J. Appl. Crystallogr.* **2011**, *44*, 1272−1276.

(44) Beal, J. H.; Etchegoin, P. G.; Tilley, R. D. Synthesis and characterisation of magnetic iron sulfide nanocrystals. *J. Solid State Chem.* **2012**, *189*, 57−62.

(45) Yund, R.; Hall, H. Hexagonal and monoclinic pyrrhotites. *Econ. Geol. Bull. Soc. Econ. Geol.* **1969**, *64*, 420−423.

(46) Shimada, K.; Mizokawa, T.; Mamiya, K.; Saitoh, T.; Fujimori, A.; Kamimura, T. Fe chalcogenides by X-ray photoemission spectroscopy. *Surf. Sci. Spectra* **1999**, *6*, 321−336.

(47) King, H.; Prewitt, C. High-pressure and high-temperature polymorphism of iron sulfide (FeS). *Acta Crystallogr., Sect. B: Struct. Crystallogr. Cryst. Chem.* **1982**, *38*, 1877−1887.

(48) Tasker, P. W. The stability of ionic crystal surfaces. *J. Phys. C: Solid State Phys.* **1979**, *12*, 4977−4984.

(49) De Leeuw, N. H.; Parker, S. C. Surface structure and morphology of calcium carbonate polymorphs calcite, aragonite, and vaterite: An atomistic approach. *J. Phys. Chem. B* **1998**, *102*, 2914−2922.

(50) Heifets, E.; Goddard, W., III; Kotomin, E.; Eglitis, R.; Borstel, G. Ab initio calculations of the SrTiO3 (110) polar surface. *Phys. Rev. B: Condens. Matter Mater. Phys.* **2004**, *69*, 035408.

(51) De Leeuw, N. H.; Parker, S. C.; Sithole, H. M.; Ngoepe, P. E. Modeling the surface structure and reactivity of pyrite: Introducing a potential model for FeS2. *J. Phys. Chem. B* **2000**, *104*, 7969−7976.

(52) Santos-Carballal, D.; Roldan, A.; de Leeuw, N. H. Early oxidation processes on the greigite Fe3S4(001) surface by water: A density functional theory study. *J. Phys. Chem. C* **2016**, *120*, 8616−8629.

(53) Santosh, K. C.; Longo, R. C.; Wallace, R. M.; Cho, K. Surface oxidation energetics and kinetics on MoS2 monolayer. *J. Appl. Phys.* **2015**, *117*, 135301.

(54) Martincova, J.; Otyepka, M.; Lazar, P. Is single layer MoS2 stable in the air? *Chem. - Eur. J.* **2017**, *23*, 13233−13239.

(55) Shi, H.; Stampfl, C. First-principles investigations of the structure and stability of oxygen adsorption and surface oxide formation at Au (111). *Phys. Rev. B: Condens. Matter Mater. Phys.* **2007**, *76*, 075327.

(56) Pedoussaut, N. M.; Lind, C. Facile synthesis of troilite. *Inorg. Chem.* **2008**, *47*, 392−394.

(57) Soon, A.; Todorova, M.; Delley, B.; Stampfl, C. Thermodynamic stability and structure of copper oxide surfaces: A first-principles investigation. *Phys. Rev. B: Condens. Matter Mater. Phys.* **2007**, *75*, 125420.

(58) Fronzi, M.; Soon, A.; Delley, B.; Traversa, E.; Stampfl, C. Stability and morphology of cerium oxide surfaces in an oxidizing environment: A first-principles investigation. *J. Chem. Phys.* **2009**, *131*, 104701.